Acta Materialia 143 (2018) 20–29

Contents lists available at ScienceDirect

Acta Materialia

journal homepage: www.elsevier.com/locate/actamat

Ni-Mn-Ga micro-trusses via sintering of 3D-printed inks containing elemental powders

Shannon L. Taylor [a, c], Ramille N. Shah [a, b, c], David C. Dunand [a, *]

[a] Department of Materials Science and Engineering, Northwestern University, 2220 Campus Dr. Cook Hall 2036, Evanston, IL, 60208, USA
[b] Department of Surgery (Transplant Division), Northwestern University, 303 E. Superior St., 11th Floor, Chicago, IL, 60611, USA
[c] Simpson Querrey Institute for BioNanotechnology in Medicine, Northwestern University, 303 E. Superior, Suite 11-131, Chicago, IL, 60611, USA

ARTICLE INFO

Article history:
Received 18 August 2017
Received in revised form
29 September 2017
Accepted 2 October 2017
Available online 3 October 2017

Keywords:
Additive manufacturing
Porosity
Magnetic shape memory alloy
Sintering
Liquid phase sintering

ABSTRACT

Ni-Mn-Ga magnetic shape memory alloy (SMA) micro-trusses, suitable for high magnetic field induced strains and/or a large magnetocaloric effect, are created via a new additive manufacturing method combining (i) 3D-printing of ~400 μm struts with an ink containing a polymer binder and elemental Ni, Mn, and Ga powders, (ii) binder burn-out and metallic powder interdiffusion and homogenization to create the final alloy, and (iii) further sintering to increase strut density. Controlled amounts of hierarchical porosity, desirable to enable twinning in this polycrystalline alloy, are achieved after sintering: (i) continuous, ~450 μm wide channels between the printed, ~300 μm diameter Ni-Mn-Ga struts and (ii) microporosity within the struts, from 50 to 200 μm voids where the largest Ga powders initially resided, and from residual 5–25 μm pores between powders due to incomplete sintering. The micro-trusses, sintered at 1000 °C for 12 h, and chemically ordered for 10 h at 700 °C, with overall porosities of 73–76%, have uniform compositions near Ni-32Mn-18Ga (at.%) and are comprised of a non-modulated martensite phase. Reversible martensite/austenite transformations between 45 and 90 °C, Curie temperatures of 85–90 °C, and saturation magnetizations of up to 56 Am^2/kg are achieved.

1. Introduction

A large magnetic shape memory effect (MSME) was discovered in 1996 by Ullakko et al. [1] in Ni_2MnGa single crystals. The low-temperature martensite phase exhibits twins whose magnetic moments rotate to align with an applied magnetic field, resulting in a magnetic field induced strain (MFIS). This MFIS is permanent when the magnetic field is removed but can be reversed when the field direction is inverted [1,2], with $>10^8$ cycles reported [3]. A thermal- or stress-induced martensitic transformation may also be achieved in these alloys, often resulting in superelastic properties [4,5]. Compared to thermally-activated shape memory alloys such as NiTi, magnetically-activated shape memory alloys exhibit much faster cycling, allowing higher frequency applications [6], making them suitable for sensor and actuator [6–8] applications including bio-medical pumps for drug delivery [9], energy harvesting devices [10,11], and small-scale fluid repulsion devices [12]. However, the largest MFIS values of up to ~10% are only reported for single crystals [2]. The slow speed of growing single-crystal Ni-Mn-Ga, the tendency for Mn evaporation, and the strong chemical segregation during single-crystal growth make polycrystalline Ni-Mn-Ga desirable [2], but their MFIS is near zero due to constraints during twinning of neighboring grains. Oligocrystals exhibit a small number of grains relative to their overall volume and they have shown MFIS values in the range of ~0.1–1% [13–15]. These values have been reported for microtextured materials formed by directional solidification from a melt [13] and replication casting [16,17] and in wires drawn using the Taylor-Ulitovsky wire drawing technique [15,18–20]. The grains span the radial cross-section of the wires, creating a bamboo grain structure [14]. However, these methods are limited to structures with high aspect ratios such as fibers and ribbons and creating larger parts is difficult.

The introduction of porosity to polycrystalline Ni-Mn-Ga increases the MFIS by reducing the twinning incompatibilities between neighboring grains [15,21–23]. Chmielus et al. reported MFIS values of 8.7% in a cast polycrystalline Ni-Mn-Ga foam using sodium aluminate as a removable spaceholder [22]. Two sizes of spaceholder particles were used to create a bimodal pore

---

* Corresponding author.
E-mail addresses: shannontaylor2018@u.northwestern.edu (S.L. Taylor), ramille-shah@northwestern.edu (R.N. Shah), dunand@northwestern.edu (D.C. Dunand).

https://doi.org/10.1016/j.actamat.2017.10.002
1359-6454/

distribution in the foam, which allowed the growth of large bamboo grains spanning the foam struts. The increased surface area and reduced grain boundary impingements in porous Ni-Mn-Ga have also been reported to enhance the magnetocaloric effect, which is important for magnetic refrigeration [24]. Such foam fabrication methods allow the creation of larger scale parts, but part geometries are limited, spaceholder removal (often by chemical dissolution) can be slow, and achieving a uniform porosity (of importance to minimize stress concentrations and grain boundary impingement) can be difficult [15,17,22–25]. Foams fabricated from pre-alloyed Ni-Mn-Ga powders produced via ball milling sinter poorly due to the large particle size, angular nature, and low interdiffusivity [26]. The use of gas atomized powders enhances sintering due to their spherical shapes [27]; however, production of such custom powders is expensive. Both foam fabrication approaches result in foams with random porosity; however, additional control over the pore architecture (size, shape, connectivity, etc.) is desired. Micro-architectured materials have improved properties compared to randomly oriented porous materials [28–32]. The creation of micro-architectured Ni-Mn-Ga would be advantageous to reduce stress concentrations and twinning impingements. Additionally, specific micro-architectures can be designed to improve specific properties in an isotropic or anisotropic manner [30,33], which cannot be achieved with foams with near equiaxed pores with random orientation.

Additive manufacturing (AM) techniques offer control over the overall geometry of the objects as well as their micro-architectures and porosity [34–38]. To date, we are aware of only two publications addressing AM of Ni-Mn-Ga alloys. Mostafaei et al. [39] and Caputo and Solomon [40] used binder jet printing and subsequent sintering of pre-alloyed powders to produce Ni-Mn-Ga foams and micro-trusses, respectively, with magnetic, microstructural, and thermal properties similar to those of bulk Ni-Mn-Ga. So far, extrusion-based 3D-printing (3DP) of metallic micro-architectured parts has not yet been used for producing micro-architectured Ni-Mn-Ga, but it is a promising alternative to powder bed-based AM techniques because it does not require removal of excess powders after printing, can be used for a wide variety of different materials, including the potential for multi-material printing from multiple print-heads, and is not subject to thermal gradients or residual stresses from the use of lasers or electron beams [36,37,41–45]. Extrusion-based 3DP of metallic inks has been used to produce Ti-6Al-4V scaffolds [46–48], steel [49], copper, iron, and nickel micro-lattices [41,50,51], and silver electrodes [52] and freeform structures [53] via the extrusion of a high-viscosity ink consisting of a polymer binder, solvents, and metallic powders: after printing, powder sintering leads to load-bearing metallic parts. Oxide or hydride inks have also been 3DP to produce metallic architectures with an additional reduction step [41,50,54–56]. Both ink-jet and ink-extrusion techniques rely solely on temperature-assisted sintering without any applied pressure, making the use of pre-alloyed Ni-Mn-Ga powders with poor sintering ability challenging [26].

Starting from elemental Ni, Mn, and Ga powder blends rather than pre-alloyed powders should improve sintering [57]. The elemental approach has been used successfully to create off-stoichiometric Ni_2MnGa thin films [58] and tubes [59] after interdiffusion and homogenization of electroplated layers. However, traditional metal additive manufacturing techniques such as selective laser sintering, binder jet printing or electron beam melting are limited to using pre-alloyed powders to manufacture Ni-Mn-Ga alloys as the incorporation of low melting Ga powders would be extremely difficult. Also, whereas Ni and Mn powders are readily available from suppliers, Ga powders are not, due to the low melting point (29 °C).

Here, we provide a novel approach wherein liquid Ga is added directly to the liquid inks and the subsequent mixing and sonication of liquid Ga in suspension results in the formation of small droplets/powders. Similar techniques have been used to produce Ga droplets for electronics [60]. We extend here the techniques we have described in Refs. [41,50] (as applied to unalloyed, pure Fe, Ni, and Cu) to produce Ni-Mn-Ga micro-trusses with controlled amounts of porosity via (i) 3D-printing of a particle-based ink containing a blend of elemental Ni, Mn, and Ga powders, (ii) interdiffusion and homogenization to create the final alloy, and (iii) further sintering to control the final porosity between and within the extruded struts comprising the micro-trusses. The microstructural, magnetic, and thermal properties of the final micro-trusses are presented.

2. Experimental procedures

Two Ni-Mn-Ga inks with nominal metallic compositions (at.%) of Ni-Mn29.5-Ga22.5 (for porosity studies) or Ni-30Mn-20.5Ga (for property characterization) were prepared using similar ink preparation methods as those reported in Refs. [41,50], but with a few modifications to accommodate the liquid Ga. First, 0.78 g of poly(lactic-*co*-glycolic) acid (PLGA; 82:18 PLA-PLG (poly-lactic acid – poly-glycolic acid) by mass; Boehringer Ingelheim, Germany) were dissolved in ~10 mL of dichloromethane (DCM; Sigma-Aldrich, USA; >99.8%) in the ink cartridge (Nordson EFD 30 cc fluid dispensing system). Then, 3.19 g of metallic Ga (99.99%, Alfa Aesar, USA) were melted and added to the ink cartridge using a polymer pipette. The Ga+PLGA slurry was then stirred using a mini-vortexer (VWR) to break up the liquid Ga drops from the pipette into smaller droplets, and then cooled in an ice water bath to solidify the Ga droplets into powders and, thus, prevent them from merging with each other in the liquid state during further ink processing and extrusion. A slurry containing (i) 7.70 g of Ni powders (Alfa Aesar, USA; 99.9% purity; 3–7 μm); (ii) 4.67 g of Mn powders (Alfa Aesar, USA; 99.6% purity; <10 μm), (iii) 0.92 g of dibutyl phthalate (Sigma-Aldrich, USA; 99%), (iv) 1.82 g of ethyl glycol dibutyl ether (EGBE; Sigma-Aldrich, USA; ≥99%), (v) 0.75 g of PLGA (~half of total polymer in ink), and (vi) ~10 mL of DCM was prepared by first dissolving the PLGA in the DCM, then adding the remaining components in a 50 mL Falcon tube, and mixing with the mini-vortexer. This Ni+Mn slurry was then poured into the ink cartridge, further mixed via the mini-vortexer, and was allowed to evaporate at room temperature until a viscosity of ~30–35 Pa·s was reached. The ratio of metallic powders to PLGA in the ink was 6:4 by volume. The inks were periodically stirred with a spatula and mini-vortexed to prevent particle settling and increase solvent evaporation.

Ni-Mn-Ga micro-trusses were created using an extrusion-based 3D-printer (Bioplotter, EnvisionTec, Germany). The liquid ink was extruded through a 400 μm diameter conical nozzle (Nordson EFD) at a pressure of 0.4–0.5 bar and a speed of ~10 mm/s. Smaller nozzle diameters clogged prior to print completion. Upon extrusion, the DCM evaporates rapidly due to the increased surface area of the struts compared to the volume of the ink in the cartridge, resulting in self-supporting structures. Micro-trusses measuring $20 \times 20 \times 4$ mm^3 (10 layers) were created by printing horizontal arrays of parallel, cylindrical struts spaced 1 mm apart, with each subsequent array rotated 90° with respect to the previous one. Smaller pieces were then cut using razor blades or 1-mm-diameter biopsy punches for the sintering studies.

The as-printed micro-trusses were first heated at 10 °C/min in a hydrogen tube furnace (MTI Corporation GSL-1500X-50HG) to 300 °C and held for 1 h to remove the PLGA binder and residual solvents, then heated to 600 °C for 2 h to partially sinter the structure, and furnace cooled under 99.999% pure H_2 gas (Airgas) at a flow rate of ~160–200 mL/min. The partially sintered micro-trusses were then encapsulated in quartz tubes with Ta foil getters and Mn pieces under a ~10^{-2} torr vacuum. The Mn pieces created a Mn atmosphere inside the quartz capsule so as to prevent evaporative losses of Mn from the micro-trusses during heat treatment. The quartz tubes were annealed for 2–12 h at 1000 °C in a box furnace (SentroTech St-1600°C-445) and then water quenched. Attempts to sinter at 1050 °C resulted in melting and loss of the 3DP micro-architecture from the formation of too much liquid phase. Finally, the encapsulated micro-trusses were annealed in a muffle furnace (Barnstead Thermolyne Type 1400) for 10 h at 700 °C to achieve chemical ordering [15,17] and then quenched in ice water.

The micro-trusses were cut in half using a diamond saw. One half was mounted in epoxy and polished using 320, 400, 600, 800, and 1200 grit SiC paper, 3 and 1 μm diamond suspensions, and a 0.05 μm alumina suspension (all from Buehler). The polished cross-sections were imaged using an inverted light microscope (Nikon MA200 Eclipse) and scanning electron microscopes (SEM, Hitachi 8030 and Hitachi 3400). Electron dispersive spectroscopy (EDS; Oxford) was performed to determine the chemical composition. The porosity within the struts was measured from optical images of the polished cross-sections using ImageJ software.

The martensite/austenite transformation and Curie temperatures were measured using a differential scanning calorimeter (DSC) at a heating/cooling rate of 10 °C/min (Mettler Toledo, Switzerland) on 5–6 mg of sample. The samples were subjected to three thermal cycles from −40 °C to 150 °C (both heating and cooling). The phase transformation temperatures were calculated from the DSC curves from the first cycle using the intersection of lines constructed tangent to the baseline and the edges of the peaks. Magnetic measurements were performed on the remaining half of the micro-trusses (~12–26 mg) using a Physical Properties Measurement System (PPMS; Quantum Designs, USA) with a VSM attachment. The magnetic field (1.5 T) was aligned perpendicular to the 3DP z-direction. The micro-trusses were then ground with a mortar and pestle and the resulting powder was used for X-Ray diffraction (XRD) using a Scintag XRD machine. Scans were collected from 35 to 130° (2θ) using Cu Kα radiation with an energy of 40 kV, a current of 20 mA, a step size of 0.05°, and a scan speed of 2 s/step.

3. Results and discussion

3.1. Incorporation of Ga into liquid inks

Fig. 1 shows SEM images of the Ni, Mn, and Ga powders used to create the inks. The as-received spherical Ni powders (Fig. 1a) are 3–7 μm and the angular Mn powders (Fig. 1b) are <10 μm in size. Due to its low melting point (29 °C), Ga powders are not commercially available, so the Ga powders were created by adding Ga liquid to a solution of PLGA dissolved in DCM and then mixing with a mini-vortexer and sonicating the solution. The milliliter-sized additions of liquid Ga break up into much smaller droplets, as shown in Fig. 1c, due to the high surface tension [61]. Some droplets have a similar size to the Ni and Mn powders (~10 μm), but most are ~50 μm in size. In a few extreme cases, the Ga droplets are larger than 100 μm. Further refinement of the Ga droplet size may be achieved by cryomilling as solid Ga is brittle [62], increasing sonication time, or through the addition of suspension stabilizing agents [60].

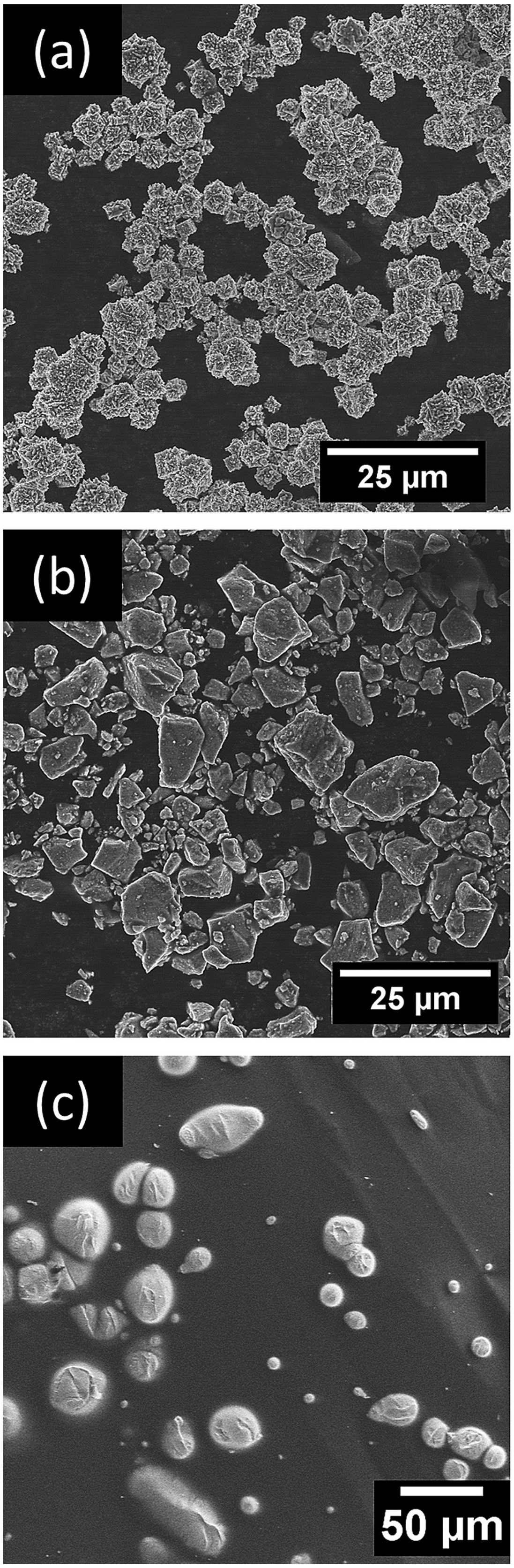

Fig. 1. SEM images of the as-received (a) Ni and (b) Mn powders, and (c) Ga powders dispersed in a PLGA + DCM slurry used in the liquid inks.

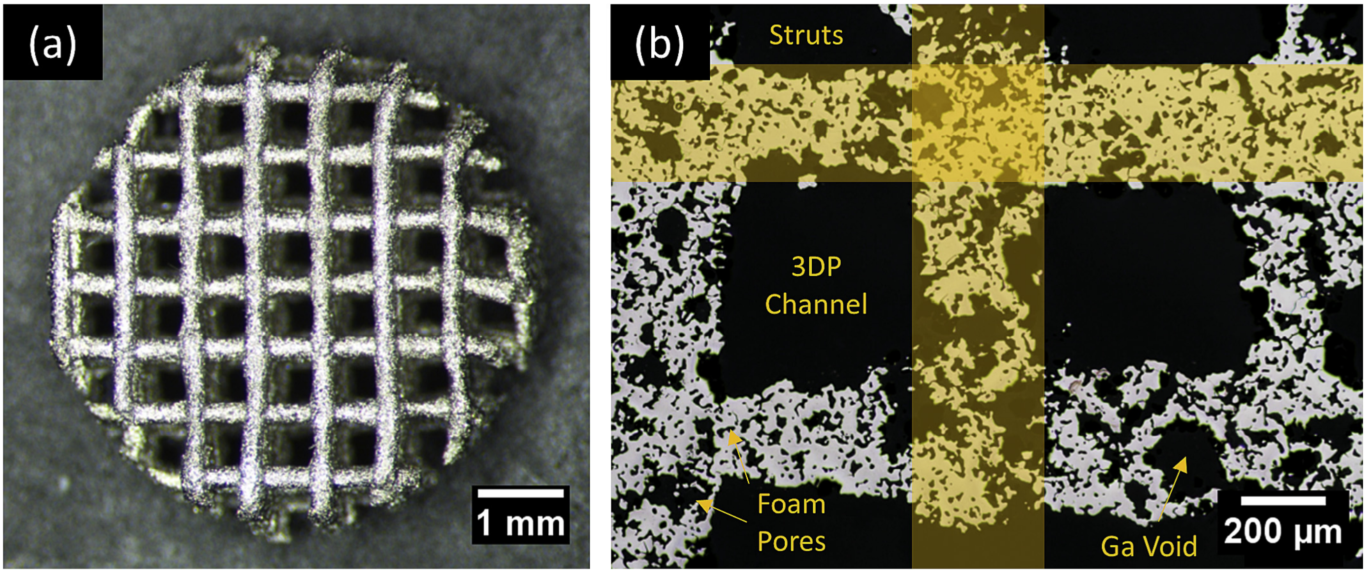

Fig. 2. (a) Photograph and (b) optical micrograph of a polished cross-section of a 3DP Ni-Mn-Ga micro-truss (after sintering at 1000 °C for 12 h and ordering at 700 °C for 10 h), showing struts and channels as well as two types of porosity (pores from incomplete sintering and voids from larger Ga powders melting and diffusing into the surrounding Ni and Mn powders) within the struts.

3.2. *Microstructure and composition*

Fig. 2a shows a 3D-printed Ni-Mn-Ga micro-truss after sintering at 1000 °C for 12 h and ordering at 700 °C for 10 h. Isotropic linear shrinkage, as measured in the x, y, and z-dimensions with respect to the 3DP direction, of ~10–15% occurred after sintering and no warping or cracking of the micro-trusses was observed. Fig. 2b is an optical micrograph of a polished cross-section of the truss shown in Fig. 2a. Three types of porosity are present (Fig. 2b): (i) ~450 μm channels between the printed struts, (ii) internal porosity (~5–25 μm) within the printed struts from incomplete sintering and PLGA removal, and (iii) internal voids within the printed struts where Ga particles initially resided within the deposited powder blend. The larger Ga powders (as compared to the Ni and Mn powders) melt at low temperatures and are expected to diffuse into the surrounding Ni and Mn powders, leaving behind larger voids, which may impact the structural integrity of the micro-trusses, but do further reduce the number of grain boundary impingements in the final alloy. In this sense, the Ga serves both as a transient spaceholder (creating porosity) and a component in the final alloy. The average porosity of the struts within the micro-truss is ~40%, while the volume fraction of struts as estimated from strut diameter (~300 μm) and channel width (~450 μm) in Fig. 2a is ~40%, assuming a circular strut cross-section. The overall micro-truss porosity is then ~73%. The high levels of porosity in the micro-trusses are similar to those exhibited by previously reported polycrystalline Ni-Mn-Ga foams with large MFIS [16,22,23,25].

Fig. 3a is a polarized light micrograph of a polished cross-section of a micro-truss sintered at 1000 °C for 12 h and ordered at 700 °C for 10 h, showing martensite twins that span the width of the grains, often terminating at the surface of the internal pores. The grains shown in Fig. 3a have an average size of ~20–25 μm, two to three times the size of the initial Ni and Mn powders, indicating that significant grain growth occurs during sintering. Small, round pores (labeled S) are present at grain triple points and larger, more tortuous pores (labeled T) surround the large grains. The hierarchical pore architecture present in the micro-trusses, the presence of martensitic grains surrounded by free volume (Fig. 3b), as well as the bamboo grains spanning full sections of short internal metallic

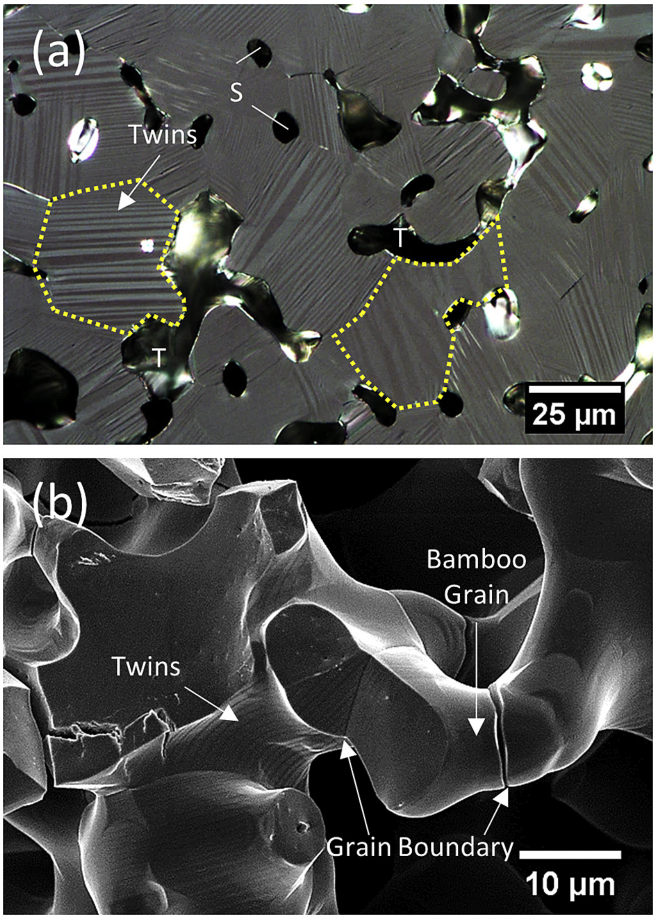

Fig. 3. (a) Polarized light optical micrograph of polished cross-section of a 3DP Ni-Mn-Ga micro-truss (sintered for at 1000 °C for 12 h and ordered at 700 °C for 10 h) showing martensite twins (arrow) spanning the grains (two of which are outlined with a dashed yellow line) and smaller rounded pores (S) and larger more tortuous pores (T). (b) SEM image of the surface of the same specimen, showing martensite twins, grain boundaries that cracked during sample cutting, and a bamboo grain.

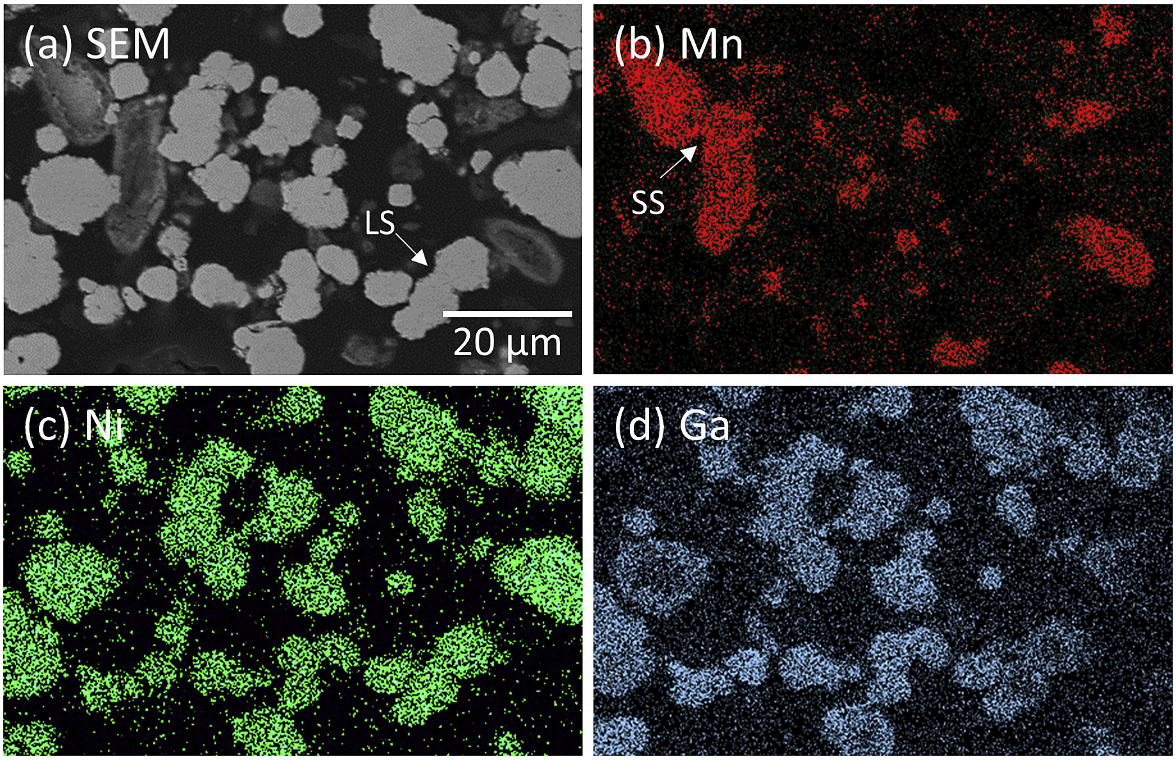

Fig. 4. (a) SEM micrograph and (b, c, d) EDS maps of Ni, Mn, and Ga distribution in a cross-section of a 3DP Ni-Mn-Ga micro-truss after debinding for 1 h at 300 °C and partial sintering for 2 h at 600 °C. Gallium preferentially diffuses into the Ni particles (lighter gray), resulting in liquid phase sintering necks (LS), while the Mn particles (darker gray) remain largely in elemental form with some solid state sintering necks (SS).

necks are prerequisites for these Ni-Mn-Ga micro-trusses to show non-negligible MFIS.

Fig. 4 shows EDS maps of Ni, Mn, and Ga for a micro-truss after the first stage of the heat treatment (PLGA removal and partial sintering for 2 h at 600 °C). The Mn powders remain largely in elemental form with limited Ga or Ni interdiffusion, and a few small sintering necks are present, as a result of solid state sintering (marked "SS" in Fig. 4). However, the Ni powders have much larger sintering necks and contain high amounts of Ga, consistent with liquid Ga wetting and diffusing into the Ni powders, and providing liquid phase sintering (marked "LS" in Fig. 4). This may be due to the higher diffusivity of Ga in Ni than in Mn, and/or the formation of a more tenacious oxide layer on the Mn powders, preventing wetting by, or interdiffusion with, liquid Ga.

Fig. 5 shows EDS line scans of foam walls in micro-trusses sintered at 1000 °C for 2 and 12 h, demonstrating that the composition is uniform across the foam walls within the struts of the micro-trusses; it is apparent that a short sintering time of 2 h at 1000 °C is sufficient for complete interdiffusion and homogenization of Ni, Mn, and Ga. Nevertheless, increasing sintering times beyond 2 h might be useful, as it leads to significant densification and grain growth. A series of cross-sections for samples sintered between 2 and 12 h at 1000 °C is presented in Fig. 6. As the sintering time increases, the internal strut porosity decreases from 61% to 40% and grains spanning the foam struts within the struts become visible between 10 and 12 h of sintering. Thus, varying the sintering time allows tailoring of the porosity and grain size within the struts, which is important for optimizing the MFIS and MCE of these micro-trusses.

Three micro-trusses (labeled 1, 2 and 3) sintered at 1000 °C for 12 h and ordered at 700 °C for 10 h were then selected for further characterization. The overall porosities of these samples are 76, 73, and 73%, respectively, and their chemical compositions are presented in Table 1. No residual carbonaceous material was observed in the EDS and SEM analysis. As shown in Fig. 7, the micro-trusses are comprised of the non-modulated (NM) martensite phase [63,64]. The spectrum for micro-truss 3 also contains several peaks for a second phase (indicated by the diamond symbol in Fig. 7), which correspond to a small volume fraction of the 14M martensite phase [65–69]. A large MFIS of 0.17% in single crystal NM martensite phase has been reported [70], but 10M or 14M martensite, can exhibit up to 7% [71] or 10% [72] MFIS, respectively, in the single crystal form. Thus, by decreasing the Mn content of the inks [73,74], it is likely that 10M or 14M martensite could be achieved.

3.3. Thermal properties

The DSC curves (first of three cycles) for the same three micro-trusses (sintered for 12 h at 1000 °C and ordered for 10 h at 700 °C) are shown in Fig. 8. The transformation temperatures for the first cycle are presented in Table 1. No hysteresis was observed and the enthalpy changes, ΔH, associated with the austenite and martensite phase transformations for all three micro-trusses on heating and cooling are ~7 J/g. The martensite start temperatures range from 60 to 83 °C and the martensite finish temperatures range from 46 to 67 °C. The austenite start temperatures range from 53 to 75 °C and the austenite finish temperatures range from 66 to 90 °C, consistent with previous reports for Ni-Mn-Ga alloys with higher Mn contents [74,75]. The broad peaks are indicative of an orthorhombic (14M) or non-modulated (NM) martensitic structure rather than tetragonal (10M) martensite [68,74]. The presence of two peaks for micro-trusses 2 and 3 for the martensite/austenite transition may indicate inter-martensitic transformations [75,76]. In the case of micro-

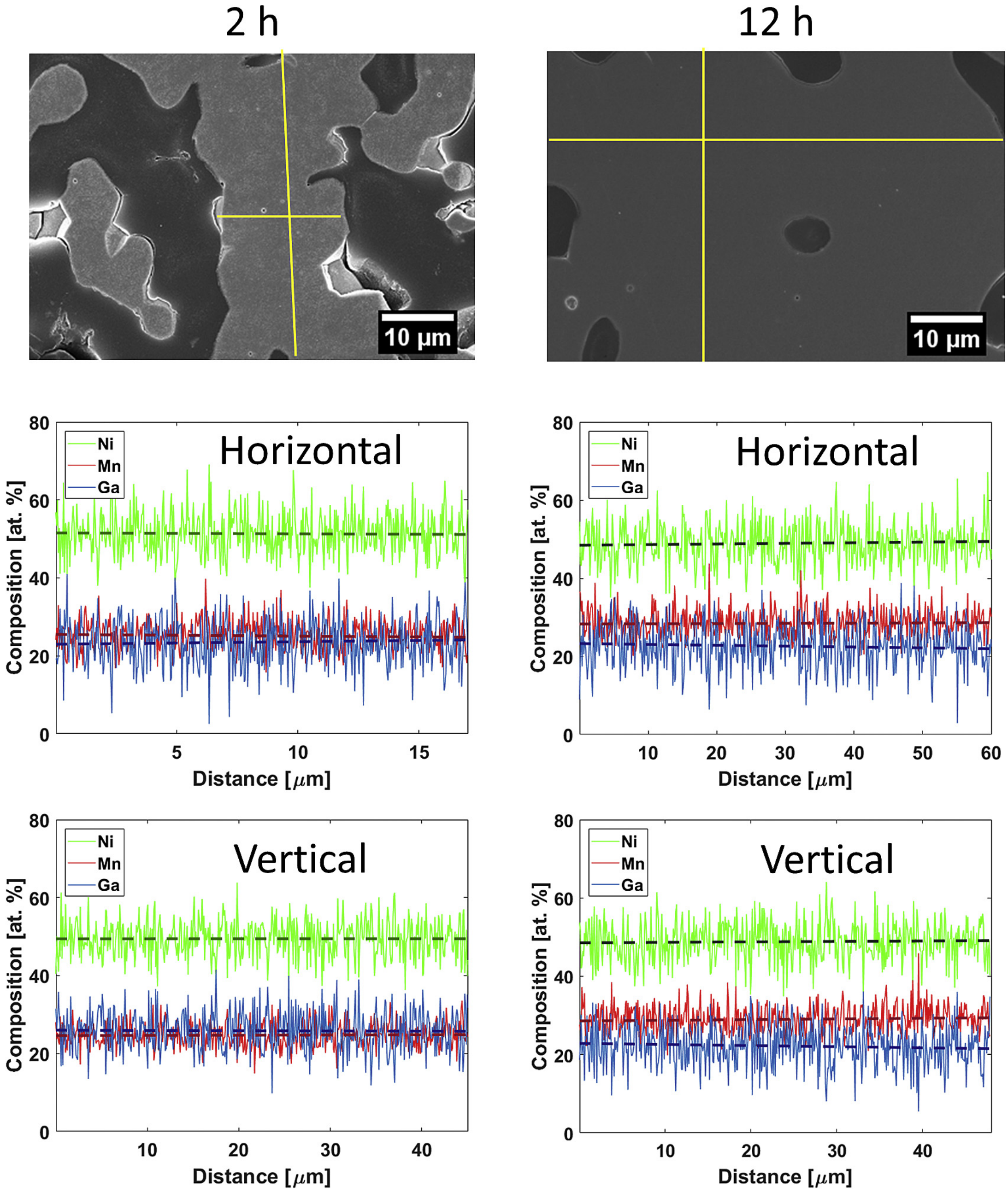

Fig. 5. SEM images and EDS line scans showing composition uniformity across foam walls in 3DP Ni-Mn-Ga micro-trusses sintered at 1000 °C for 2 and 12 h. The dashed lines are lines of best fit for the compositions.

truss 3, two martensite phases are present in the XRD spectrum. In micro-trusses 1 (cooling) and 3 (heating and cooling), a small peak corresponding to the Curie temperature is visible at 81 and 86 °C, respectively. In micro-truss 2, the peak corresponding to the Curie temperature is not visible, because it likely overlaps with the austenite/martensite peaks. However, all analyzed samples were ferromagnetic at room temperature (as determined by testing the response of the sample to a 3 × 3x1 cm^3 Fe-Nd-B magnet) and the Curie temperatures were further determined from the magneto-thermal measurements as discussed in Section 3.4.

3.4. Magnetic properties

Fig. 9 shows the magnetization vs. temperature curves for micro-trusses 1–3. The Curie temperatures determined from the magnetic measurements are 85, 91, and 95 °C, respectively, which are consistent with the Curie temperatures measured via DSC. For micro-truss 2, the measured Curie temperature is 91 °C, which supports the hypothesis that the austenite/martensite peaks in the DSC curve shown in Fig. 8 overlap with the small peak corresponding to the Curie temperature.

Magnetization loops were measured at 27 °C (300 K) for the three micro-trusses, as shown in Fig. 10. A very narrow magnetic hysteresis was observed (coercivities ~5 mT). Saturation magnetizations of 48.5, 48.0, and 56.4 Am^2/kg were measured for micro-trusses 1, 2, 3, respectively. Murray et al. [77] and Jin et al. [78] measured and predicted, respectively, magnetic saturations of 20–50 Am^2/kg for Ni-Mn-Ga alloys with similar compositions

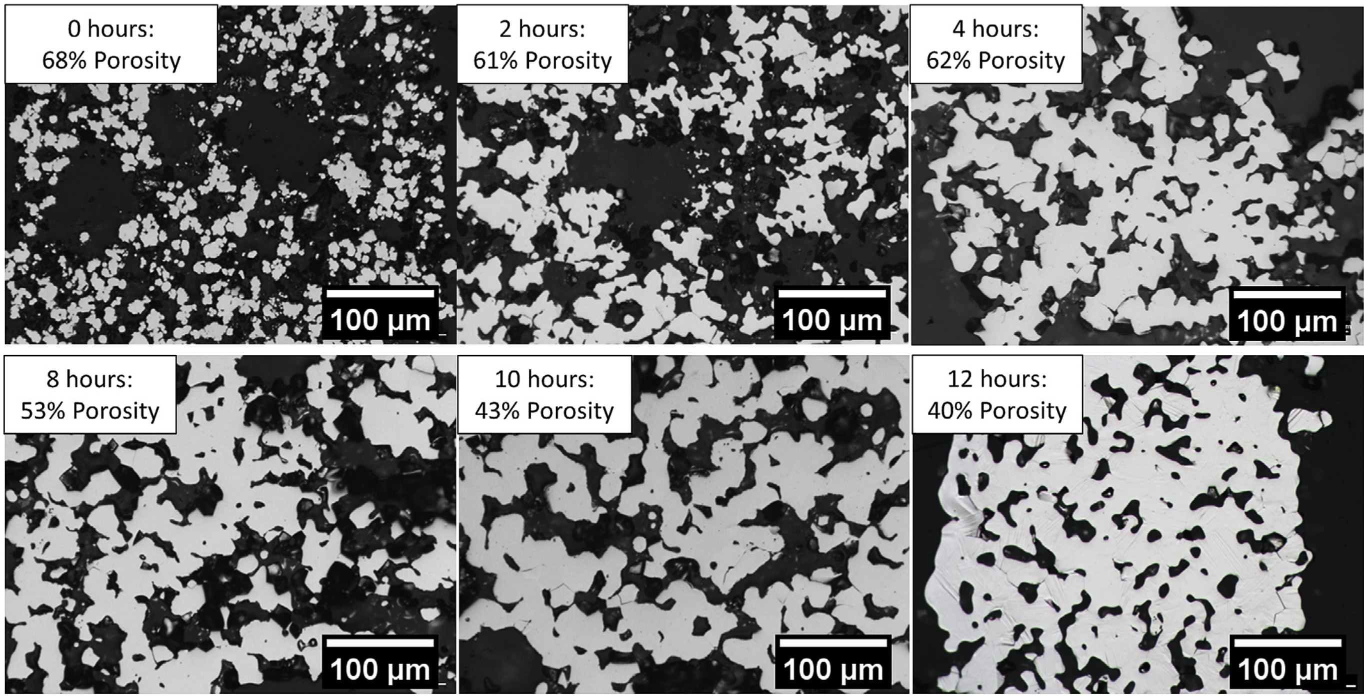

Fig. 6. Optical micrographs of polished cross-sections of 3DP micro-trusses after debinding and partial sintering (0 h) followed by sintering at 1000 °C for 2–12 h. The porosities are measured within the micro-truss struts and do not include the 3DP channels.

Table 1
Composition, thermal, and magnetic properties of 3DP Ni-Mn-Ga micro-trusses after sintering at 1000 °C for 12 h and ordering at 700 °C for 10 h.

Micro-truss	Composition				Thermal Properties						Magnetic Properties			
	Ni (at. %)	Mn (at. %)	Ga (at. %)	valence electrons/atom	Cooling			Heating			Magnetic Saturation (Am^2/kg)	Coercivity H_c (mT)	Remnant Magnetization M_r (Am^2/kg)	Curie Temperature T_c (°C)
					M_s (°C)	M_f (°C)	T_c (°C)	A_s (°C)	A_f (°C)	T_c (°C)				
1	49.8 ± 0.4	32.3 ± 0.3	17.9 ± 0.5	7.78	75.5	67	81	75	83	–	48.5	5.0	2.0	85
2	50.3 ± 0.6	31.6 ± 0.6	18.1 ± 0.9	7.79	82.5	68	–	75	90	–	48.0	4.6	2.3	91
3	49.8 ± 0.3	32.0 ± 0.4	18.2 ± 0.4	7.77	59.5	45.5	86	52.5	65.5	88.5	56.4	4.8	1.4	95

(valence-electron-per-atom ~ 7.7–7.8) to the 3DP micro-trusses reported here. The measured saturation magnetizations for the 3DP micro-trusses are in the upper range of these literature values and near that of bulk, single crystal Ni-Mn-Ga reported by Heckzo et al. [79], consistent with full homogenization of the micro-trusses. Magnetic saturations of 68.4 Am^2/kg and ~60 Am^2/kg have been reported for polycrystalline Ni-Mn-Ga foams produced by binder jet printing and subsequent sintering heat treatment [39] and microtubes created by the diffusion of Ga and Mn into a Ni microtube [59], respectively.

Preliminary testing of the micro-trusses sintered at 1000 °C for 12 h did not produce a non-negligible MFIS; however, the porosity of the present micro-trusses could be further increased by reducing sintering time and temperature, by changing 3DP parameters such as inter-strut distance or nozzle diameter and/or by acid dissolution, as performed by Ref. [16]. Increasing the porosity would then reduce the grain boundary constraints, enhance twinning and lead to measurable MFIS. Additionally, trace impurities in the initial powders or from the removal of the polymer binder and residual solvents may negatively affect MSME.

4. Conclusions

A novel additive manufacturing method for Ni-Mn-Ga micro-trusses is presented, whereby (i) a micro-truss is created via extrusion-based 3D-printing of liquid inks containing elemental Ni, Mn, and Ga powders and a polymer binder, and (ii) the micro-truss is annealed to remove the binder and residual solvents, and then interdiffuse the elements to achieve a homogenous composition and partial sintering. The resulting micro-trusses exhibit high levels of porosity (~73–76%) from a combination of (i) ~ 450 μm 3DP macro-channels, (ii) ~ 50–100 μm voids resulting from Ga particles melting at low temperature and diffusing into the surrounding Ni and Mn powders, and (iii) ~ 5–25 μm pores from incomplete sintering. Uniform compositions are obtained via interdiffusion of the elemental powders throughout the micro-trusses upon aging at 1000 °C for 2 h. Significant grain growth (20–25 μm grains) is achieved after 12 h of sintering. Reversible martensite/austenite transformations occur between 46 and 90 °C for the three micro-trusses presented here. XRD analysis indicates that non-modulated martensite is the primary phase present in the

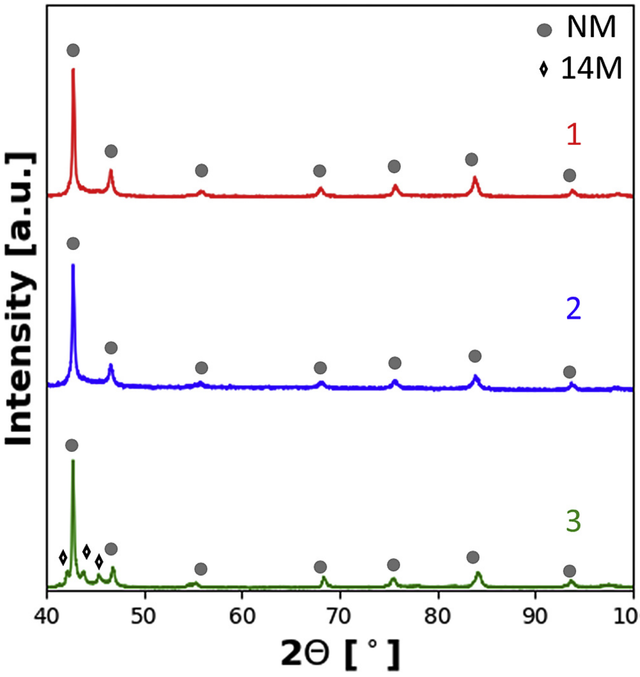

Fig. 7. XRD patterns for 3DP Ni-Mn-Ga micro-trusses 1–3 after sintering at 1000 °C for 12 h and ordering at 700 °C for 10 h. Peaks corresponding to the non-modulated (NM) and 14M martensite phases are labeled.

micro-trusses. Saturation magnetizations as high as 56 Am^2/kg were achieved. This novel 3D-printing approach for fabricating porous, polycrystalline Ni-Mn-Ga micro-trusses is promising for large magnetic shape memory or magnetocaloric effects necessary for actuator, micro-pump, power harvesting or magnetic refrigeration applications.

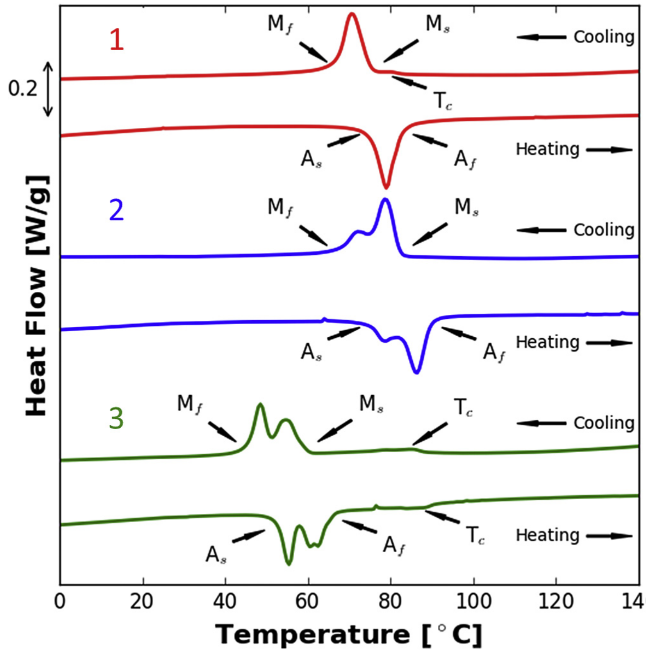

Fig. 8. DSC curves for 3DP Ni-Mn-Ga micro-trusses 1–3 after sintering at 1000 °C for 12 h and ordering at 700 °C for 10 h. The martensite/austenite start and finish temperatures (M_s/A_s; M_f/A_f) and Curie temperature (T_c), if detected, are labeled. There are two peaks for micro-trusses 2 and 3 indicative of an intermediate martensitic phase transformation.

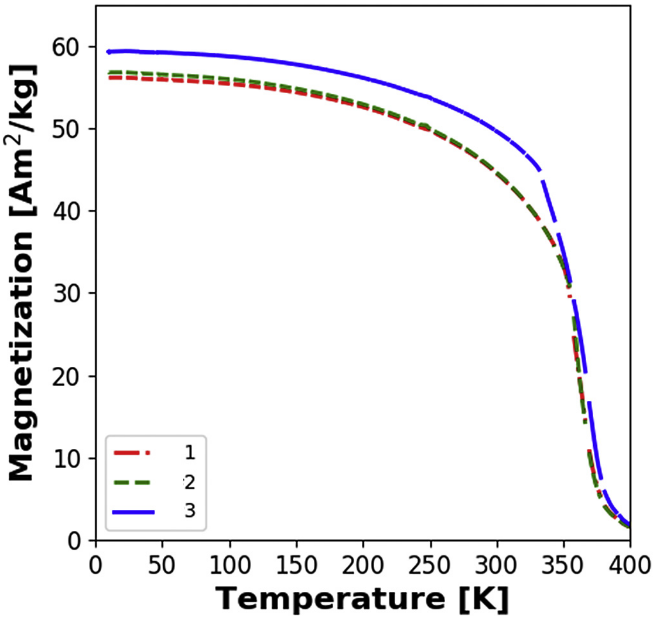

Fig. 9. Magnetization vs. temperature curves for 3DP Ni-Mn-Ga micro-trusses 1–3 after sintering at 1000 °C for 12 h and ordering at 700 °C for 10 h.

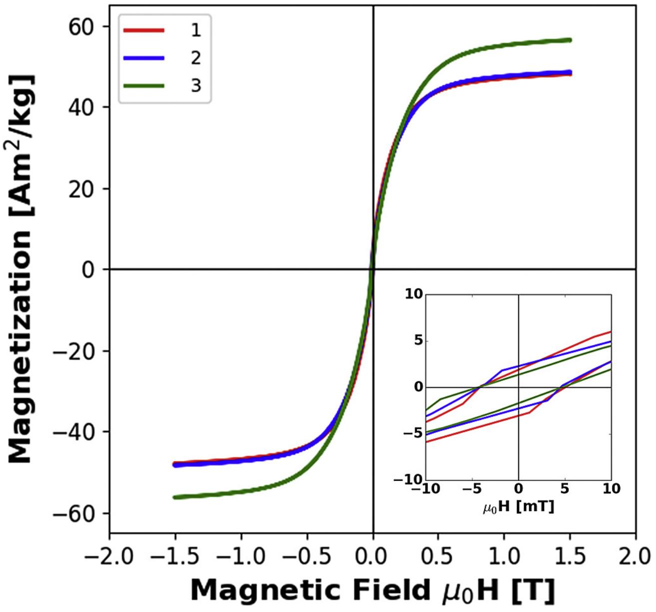

Fig. 10. Magnetic hysteresis loops at ambient temperature for 3DP Ni-Mn-Ga micro-trusses 1–3 after sintering at 1000 °C for 12 h and ordering at 700 °C for 10 h. The inset shows a magnified view of the origin.

Conflicts of interest

None.

Acknowledgements

The authors acknowledge financial support from National Science Foundation Grant No. 1207282 and the National Science Foundation Graduate Fellowship Program. This work made use of the EPIC facility of Northwestern University's NUANCE Center, which received support from the Soft and Hybrid Nanotechnology Experimental (SHyNE) Resource (NSF ECCS-1542205), the MRSEC program (NSF DMR-1121262) at the Materials Research Center, the International Institute for Nanotechnology (IIN), the Keck Foundation, and the State of Illinois, through the IIN, and the Materials Characterization Laboratory (MatCI) and J.B. Cohen X-Ray Diffraction Facility, which received support from the MRSEC program (NSF DMR-1121262). The authors thank Quantum Designs for performing the magnetic measurements in this work, Dr. Adam E. Jakus (Northwestern University) for assistance with the 3D-printing, and Prof. Peter Müllner at Boise State University for his numerous, insightful discussions as well as the preliminary MFIS measurements.

References

[1] K. Ullakko, J.K. Huang, C. Kantner, R.C. O'Handley, V.V. Kokorin, Large magnetic-field-induced strains in Ni2MnGa single crystals, Appl. Phys. Lett. 69 (1996) 1966–1968, https://doi.org/10.1063/1.117637.

[2] D.C. Dunand, P. Müllner, Size effects on magnetic actuation in Ni-Mn-Ga shape-memory alloys, Adv. Mater 23 (2011) 216–232, https://doi.org/10.1002/adma.201002753.

[3] M. Chmielus, V.A. Chernenko, W.B. Knowlton, G. Kostorz, P. Mullner, Training, constraints, and high-cycle magneto-mechanical properties of Ni-Mn-Ga magnetic shape-memory alloys, Eur. Phys. J. Spec. Top. 158 (2008) 79–85, https://doi.org/10.1140/epjst/e2008-00657-3.

[4] M.F. Qian, X.X. Zhang, C. Witherspoon, J.F. Sun, P. Müllner, Superelasticity and shape memory effects in polycrystalline Ni-Mn-Ga microwires, J. Alloys Compd. 577 (2013) S296–S299, https://doi.org/10.1016/j.jallcom.2011.10.117.

[5] Z.L. Wang, P. Zheng, Z.H. Nie, Y. Ren, Y.D. Wang, P. Müllner, D.C. Dunand, Superelasticity by reversible variants reorientation in a Ni-Mn-Ga microwire with bamboo grains, Acta Mater 99 (2015) 373–381, https://doi.org/10.1016/j.actamat.2015.08.002.

[6] S.A. Wilson, R.P.J. Jourdain, Q. Zhang, R.A. Dorey, C.R. Bowen, M. Willander, Q.U. Wahab, M. Willander, S.M. Al-hilli, O. Nur, E. Quandt, C. Johansson, E. Pagounis, M. Kohl, J. Matovic, B. Samel, W. van der Wijngaart, E.W.H. Jager, D. Carlsson, Z. Djinovic, M. Wegener, C. Moldovan, E. Abad, M. Wendlandt, C. Rusu, K. Persson, New materials for micro-scale sensors and actuators. An engineering review, Mater. Sci. Eng. R. Rep. 56 (2007) 1–129, https://doi.org/10.1016/j.mser.2007.03.001.

[7] B. Krevet, V. Pinneker, M. Kohl, A magnetic shape memory foil actuator loaded by a spring, Smart Mater. Struct. 21 (2012) 94013, https://doi.org/10.1088/0964-1726/21/9/094013.

[8] H.E. Karaca, I. Karaman, B. Basaran, Y. Ren, Y.I. Chumlyakov, H.J. Maier, Magnetic field-induced phase transformation in NiMnCoIn magnetic shape-memory alloys — a new actuation mechanism with large work output, Adv. Funct. Mater 19 (2009) 983–998, https://doi.org/10.1002/adfm.200801322.

[9] S. Barker, E. Rhoads, P. Lindquist, M. Vreugdenhil, P. Mullner, Magnetic shape memory micropump for submicroliter intracranial drug delivery in rats, J. Med. Device 10 (2016), https://doi.org/10.1115/1.4034576.

[10] I. Karaman, B. Basaran, H.E. Karaca, A.I. Karsilayan, Y.I. Chumlyakov, Energy harvesting using martensite variant reorientation mechanism in a NiMnGa magnetic shape memory alloy, Appl. Phys. Lett. 90 (2007), https://doi.org/10.1063/1.2721143.

[11] N.M. Bruno, C. Ciocanel, H.P. Feigenbaum, A. Waldauer, A theoretical and experimental investigation of power harvesting using the NiMnGa martensite reorientation mechanism, Smart Mater. Struct. 21 (2012), https://doi.org/10.1088/0964-1726/21/9/094018.

[12] O.Y. Kanner, D. Shilo, J. Sheng, R.D. James, Y. Ganor, Ferromagnetic shape memory flapper for remotely actuated propulsion systems, Smart Mater. Struct. 22 (2013), https://doi.org/10.1088/0964-1726/22/8/085030.

[13] U. Gaitzsch, M. Pötschke, S. Roth, B. Rellinghaus, L. Schultz, A 1% magnetostrain in polycrystalline 5M Ni–Mn–Ga, Acta Mater 57 (2009) 365–370, https://doi.org/10.1016/j.actamat.2008.09.017.

[14] N. Scheerbaum, O. Heczko, J. Liu, D. Hinz, L. Schultz, O. Gutfleisch, Magnetic field-induced twin boundary motion in polycrystalline Ni-Mn-Ga fibres, New J. Phys. 10 (2008), https://doi.org/10.1088/1367-2630/10/7/073002.

[15] Y. Boonyongmaneerat, M. Chmielus, D.C. Dunand, P. Müllner, Increasing magnetoplasticity in polycrystalline Ni-Mn-Ga by reducing internal constraints through porosity, Phys. Rev. Lett. 99 (2007) 1–4, https://doi.org/10.1103/PhysRevLett.99.247201.

[16] C. Witherspoon, P. Zheng, M. Chmielus, D.C. Dunand, P. Müllner, Effect of porosity on the magneto-mechanical behavior of polycrystalline magnetic shape-memory Ni-Mn-Ga foams, Acta Mater 92 (2015) 64–71, https://doi.org/10.1016/j.actamat.2015.03.038.

[17] P. Zheng, N.J. Kucza, Z. Wang, P. Mullner, D.C. Dunand, Effect of directional solidification on texture and magnetic-field-induced strain in Ni-Mn-Ga foams with coarse grains, Acta Mater 86 (2015) 95–101, https://doi.org/10.1016/j.actamat.2014.12.005.

[18] V. Zhukova, V. Rodionova, L. Fetisov, A. Grunin, A. Goikhman, A. Torcunov, A. Aronin, G. Abrosimova, A. Kiselev, N. Perov, A. Granovsky, T. Ryba, S. Michalik, Magnetic properties of heusler-type microwires and thin films, IEEE Trans. Magn. 50 (2014) 4–7, https://doi.org/10.1109/TMAG.2014.2324494.

[19] V. Rodionova, M. Ilyn, A. Granovsky, N. Perov, V. Zhukova, G. Abrosimova, A. Aronin, A. Kiselev, A. Zhukov, Internal stress induced texture in Ni-Mn-Ga based glass-covered microwires, J. Appl. Phys. 114 (2013), https://doi.org/10.1063/1.4822168.

[20] A. Zhukov, C. Garcia, M. Ilyn, R. Varga, J.J. Del Val, A. Granovsky, V. Rodionova, M. Ipatov, V. Zhukova, Magnetic and transport properties of granular and Heusler-type glass-coated microwires, J. Magn. Magn. Mater 324 (2012) 3558–3562, https://doi.org/10.1016/j.jmmm.2012.02.089.

[21] M. Chmielus, C. Witherspoon, R.C. Wimpory, A. Paulke, A. Hilger, X. Zhang, D.C. Dunand, P. Mullner, Magnetic-field-induced recovery strain in polycrystalline Ni–Mn–Ga foam, J. Appl. Phys. 108 (2010), https://doi.org/10.1063/1.3524503.

[22] M. Chmielus, X.X. Zhang, C. Witherspoon, D.C. Dunand, P. Müllner, P. Muellner, Giant magnetic-field-induced strains in polycrystalline Ni-Mn-Ga foams, Nat. Mater 8 (2009) 863–866, https://doi.org/10.1038/nmat2527.

[23] F. Nilsén, J. Lehtonen, Y. Ge, I. Aaltio, S.-P. Hannula, Highly porous spark plasma sintered Ni-Mn-Ga structures, Scr. Mater 139 (2017) 148–151, https://doi.org/10.1016/j.scriptamat.2017.06.040.

[24] C.P. Sasso, P. Zheng, V. Basso, P. Müllner, D.C. Dunand, Enhanced field induced martensitic phase transition and magnetocaloric effect in Ni55Mn20Ga25 metallic foams, Intermetallics 19 (2011) 952–956, https://doi.org/10.1016/j.intermet.2011.02.015.

[25] X.X. Zhang, C. Witherspoon, P. Müllner, D.C. Dunand, Effect of pore architecture on magnetic-field-induced strain in polycrystalline Ni–Mn–Ga, Acta Mater 59 (2011) 2229–2239, https://doi.org/10.1016/j.actamat.2010.12.026.

[26] P. Zheng, Thesis Processing and Characterization of Ni-Mn-Ga Shape-memory Fibers and Foams, Northwestern University, 2013.

[27] F. Nilsen, I. Aaltio, Y. Ge, T. Lindroos, S.-P. Hannula, Characterization of gas atomized Ni-Mn-Ga powders, Mater. Today Proc. 2 (2015) 879–882, https://doi.org/10.1016/j.matpr.2015.07.422.

[28] T.A. Schaedler, A.J. Jacobsen, A. Torrents, A.E. Sorensen, J. Lian, J.R. Greer, L. Valdevit, W.B. Carter, Ultralight metallic microlattices, Science 334 (2011) 962–965, https://doi.org/10.1126/science.1211649.

[29] A.G. Evans, J.W. Hutchinson, M.F. Ashby, Multifunctionality of cellular metal systems, Prog. Mater. Sci. 43 (1998) 171–221, https://doi.org/10.1016/S0079-6425(98)00004-8.

[30] L. Valdevit, A.J. Jacobsen, J.R. Greer, W.B. Carter, Protocols for the optimal design of multi-functional cellular structures: from hypersonics to microarchitected materials, J. Am. Ceram. Soc. 94 (2011) 1–20, https://doi.org/10.1111/j.1551-2916.2011.04599.x.

[31] A. Torrents, T.A. Schaedler, A.J. Jacobsen, W.B. Carter, L. Valdevit, Characterization of nickel-based microlattice materials with structural hierarchy from the nanometer to the millimeter scale, Acta Mater 60 (2012) 3511–3523, https://doi.org/10.1016/j.actamat.2012.03.007.

[32] M. Ashby, Designing architectured materials, Scr. Mater 68 (2013) 4–7, https://doi.org/10.1016/j.scriptamat.2012.04.033.

[33] A.G. Evans, J.W. Hutchinson, N.A. Fleck, M.F. Ashby, H.N.G. Wadley, The topological design of multifunctional cellular metals, Prog. Mater. Sci. 46 (2001) 309–327, https://doi.org/10.1016/S0079-6425(00)00016-5.

[34] L.E. Murr, S.M. Gaytan, D.A. Ramirez, E. Martinez, J. Hernandez, K.N. Amato, P.W. Shindo, F.R. Medina, R.B. Wicker, Metal fabrication by additive manufacturing using laser and electron beam melting technologies, J. Mater. Sci. Technol. 28 (2012) 1–14, https://doi.org/10.1016/S1005-0302(12)60016-4.

[35] L.E. Murr, E. Martinez, K.N. Amato, S.M. Gaytan, J. Hernandez, D.A. Ramirez, P.W. Shindo, F. Medina, R.B. Wicker, Fabrication of metal and alloy components by additive manufacturing: examples of 3D materials science, J. Mater. Res. Technol. 1 (2012) 42–54, https://doi.org/10.1016/S2238-7854(12)70009-1.

[36] D.D. Gu, W. Meiners, K. Wissenbach, R. Poprawe, Laser additive manufacturing of metallic components: materials, processes and mechanisms, Int. Mater. Rev. 57 (2012) 133–164, https://doi.org/10.1179/1743280411Y.0000000014.

[37] W.E. Frazier, Metal additive manufacturing: a review, J. Mater. Eng. Perform. 23 (2014) 1917–1928, https://doi.org/10.1007/s11665-014-0958-z.

[38] R.D. Farahani, K. Chizari, D. Therriault, Three-dimensional printing of freeform helical microstructures: a review, Nanoscale 6 (2014) 10470–10485, https://doi.org/10.1039/C4NR02041C.

[39] A. Mostafaei, K.A. Kimes, E.L. Stevens, J. Toman, Y.L. Krimer, K. Ullakko, M. Chmielus, Microstructural evolution and magnetic properties of binder jet additive manufactured Ni-Mn-Ga magnetic shape memory foam, Acta Mater 131 (2017) 482–490, https://doi.org/10.1016/j.actamat.2017.04.010.

[40] M.P. Caputo, C.V. Solomon, A facile method for producing porous parts with complex geometries from ferromagnetic Ni-Mn-Ga shape memory alloys, Mater. Lett. 200 (2017) 87–89, https://doi.org/10.1016/j.matlet.2017.04.112.

[41] A.E. Jakus, S.L. Taylor, N.R. Geisendorfer, D.C. Dunand, R.N. Shah, Metallic architectures from 3D-printed powder-based liquid inks, Adv. Funct. Mater 25 (2015) 6985–6995, https://doi.org/10.1002/adfm.201503921.

[42] M.Y.N. Jock, E. Camposilvan, L. Gremillard, E. Maire, D. Fabrègue, D. Chicot, K. Tabalaiev, J. Adrien, Characterization of 100Cr6 lattice structures produced by robocasting, Mater. Des. (2017), https://doi.org/10.1016/

j.matdes.2017.02.066.
[43] J.A. Lewis, Direct ink writing of 3D functional materials, Adv. Funct. Mater 16 (2006) 2193–2204, https://doi.org/10.1002/adfm.200600434.
[44] J.A. Lewis, G.M. Gratson, Direct writing in three dimensions, Mater. Today (2004) 32–39, https://doi.org/10.1016/S1369-7021(04)00344-X. July/Augus.
[45] C. Yan, L. Hao, A. Hussein, D. Raymont, Evaluations of cellular lattice structures manufactured using selective laser melting, Int. J. Mach. Tools Manuf. 62 (2012) 32–38, https://doi.org/10.1016/j.ijmachtools.2012.06.002.
[46] J.P. Li, J.R. De Wijn, C.A. Van Blitterswijk, K. De Groot, Porous Ti6Al4V scaffolds directly fabricated by 3D fibre deposition technique: effect of nozzle diameter, J. Mater. Sci. Mater. Med. 16 (2005) 1159–1163, https://doi.org/10.1007/s10856-005-4723-6.
[47] J.P. Li, J.R. De Wijn, C.A. Van Blitterswijk, K. de Groot, The effect of scaffold architecture on properties of direct 3D fiber deposition of porous Ti6Al4V for orthopedic implants, J. Biomed. Mater. Res. - Part A 92 (2009) 33–42, https://doi.org/10.1002/jbm.a.32330.
[48] J.P. Li, J.R. de Wijn, C.A. Van Blitterswijk, K. de Groot, Porous Ti6Al4V scaffold directly fabricating by rapid prototyping: preparation and in vitro experiment, Biomaterials 27 (2006) 1223–1235, https://doi.org/10.1016/j.biomaterials.2005.08.033.
[49] M. Yetna N'Jock, E. Camposilvan, L. Gremillard, E. Maire, D. Fabrègue, D. Chicot, K. Tabalaiev, J. Adrien, Characterization of 100Cr6 lattice structures produced by robocasting, Mater. Des. 121 (2017) 345–354, https://doi.org/10.1016/j.matdes.2017.02.066.
[50] S.L. Taylor, A.E. Jakus, R.N. Shah, D.C. Dunand, Iron and nickel cellular structures by sintering of 3D-printed oxide or metallic particle inks, Adv. Eng. Mater (2016), https://doi.org/10.1002/adem.201600365.
[51] L. Ren, X. Zhou, Z. Song, C. Zhao, Q. Liu, J. Xue, X. Li, Process parameter optimization of extrusion-based 3D metal printing utilizing PW-LDPE-SA binder system, Mater. (Basel) 10 (2017), https://doi.org/10.3390/ma10030305.
[52] B.Y. Ahn, E.B. Duoss, M.J. Motala, X. Guo, S.-I. Park, Y. Xiong, J. Yoon, R.G. Nuzzo, J.A. Rogers, J.A. Lewis, Omnidirectional printing of flexible, stretchable, and spanning silver microelectrodes, Science 80 (323) (2009) 1590–1593, https://doi.org/10.1126/science.1168375.
[53] M.A. Skylar-Scott, S. Gunasekaran, J.A. Lewis, Laser-assisted direct ink writing of planar and 3D metal architectures, Proc. Natl. Acad. Sci. 113 (2016) 6137–6142, https://doi.org/10.1073/pnas.1525131113.
[54] E. Hong, B.Y. Ahn, D. Shoji, J.A. Lewis, D.C. Dunand, Microstructure and mechanical properties of reticulated titanium scrolls, Adv. Eng. Mater 13 (2011) 1122–1127, https://doi.org/10.1002/adem.201100082.
[55] W.K.C. Yung, B. Sun, Z. Meng, J. Huang, Y. Jin, H.S. Choy, Z. Cai, G. Li, C.L. Ho, J. Yang, W.Y. Wong, Additive and photochemical manufacturing of copper, Sci. Rep. 6 (2016) 2–10, https://doi.org/10.1038/srep39584.
[56] B.Y. Ahn, D. Shoji, C.J. Hansen, E. Hong, D.C. Dunand, J.A. Lewis, Printed origami structures, Adv. Mater 22 (2010) 2251–2554, https://doi.org/10.1002/adma.200904232.
[57] R.M. German, Powder Metallurgy Science, second ed., Metal Powder Industries Federation, Princeton, New Jersey, USA, 1994.
[58] U. Gaitzsch, J. Drache, K. McDonald, P. Müllner, P. Lindquist, Obtaining of Ni-Mn-Ga magnetic shape memory alloy by annealing electrochemically deposited Ga/Mn/Ni layers, Thin Solid Films 522 (2012) 171–174, https://doi.org/10.1016/j.tsf.2012.08.019.
[59] P. Zheng, P. Lindquist, B. Yuan, P. Müllner, D.C. Dunand, Fabricating Ni–Mn–Ga microtubes by diffusion of Mn and Ga into Ni tubes, Intermetallics 49 (2014) 70–80, https://doi.org/10.1016/j.intermet.2014.01.014.
[60] K. Du, E. Glogowski, M.T. Tuominen, T. Emrick, T.P. Russell, A.D. Dinsmore, Self-assembly of gold nanoparticles on gallium droplets: controlling charge transport through microscopic devices, Langmuir 29 (2013) 13640–13646, https://doi.org/10.1021/la403263z.
[61] C. Ladd, J.H. So, J. Muth, M.D. Dickey, 3D printing of free standing liquid metal microstructures, Adv. Mater 25 (2013) 5081–5085, https://doi.org/10.1002/adma.201301400.
[62] E.M. Savitsky, The Influence of Temperature on the Mechanical Properties of Metals and Alloys, Stanford University Press, Stanford, California, 1961.
[63] B. Wedel, M. Suzuki, Y. Murakami, C. Wedel, T. Suzuki, D. Shindo, K. Itagaki, Low temperature crystal structure of Ni–Mn–Ga alloys, J. Alloys Compd 290 (1999) 137–143, https://doi.org/10.1016/S0925-8388(99)00198-X.
[64] J. Pons, V.A. Chernenko, R. Santamarta, E. Cesari, Crystal structure of martensitic phases in Ni-Mn-Ga shape memory alloys, Acta Mater 48 (2000) 3027–3038, https://doi.org/10.1016/S1359-6454(00)00130-0.
[65] L. Righi, F. Albertini, E. Villa, A. Paoluzi, G. Calestani, V. Chernenko, S. Besseghini, C. Ritter, F. Passaretti, Crystal structure of 7M modulated Ni – Mn – Ga martensitic phase, Acta Mater 56 (2008) 4529–4535, https://doi.org/10.1016/j.actamat.2008.05.010.
[66] L. Righi, F. Albertini, G. Calestani, L. Pareti, A. Paoluzi, C. Ritter, P.A. Algarabel, L. Morellon, M.R. Ibarra, Incommensurate modulated structure of the ferromagnetic shape-memory Ni 2 MnGa martensite, J. Solid State Chem. 179 (2006) 3525–3533, https://doi.org/10.1016/j.jssc.2006.07.005.
[67] L. Righi, F. Albertini, L. Pareti, A. Paoluzi, G. Calestani, Commensurate and incommensurate "‘ 5M ’" modulated crystal structures in Ni – Mn – Ga martensitic phases, Acta Mater 55 (2007) 5237–5245, https://doi.org/10.1016/j.actamat.2007.05.040.
[68] M.L. Richard, J. Feuchtwanger, S.M. Allen, R.C. O'handley, P. Lázpita, J.M. Barandiaran, Martensite transformation in Ni-Mn-Ga ferromagnetic shape-memory alloys, Metall. Mater. Trans. A 38A (2007) 777–780, https://doi.org/10.1007/s11661-007-9097-6.
[69] P.J. Brown, J. Crangle, T. Kanomata, M. Matsumoto, K.-U. Neumann, B. Ouladdiaf, K.R.A. Ziebeck, The crystal structure and phase transitions of the magnetic shape memory compound Ni2MnGa, J. Phys. Condens. Matter 14 (2002) 10159–10171, https://doi.org/10.1088/0953-8984/14/43/313.
[70] V.A. Chernenko, M. Chmielus, P. Müllner, Large magnetic-field-induced strains in Ni – Mn – Ga nonmodulated martensite, Appl. Phys. Lett. 95 (2009), https://doi.org/10.1063/1.3227661.
[71] E. Pagounis, R. Chulist, M.J. Szczerba, M. Laufenberg, Over 7 % magnetic field-induced strain in a Ni-Mn-Ga five-layered martensite, Appl. Phys. Lett. 105 (2014), https://doi.org/10.1063/1.4892633.
[72] A. Sozinov, A.A. Likhachev, N. Lanska, K. Ullakko, Giant magnetic-field-induced strain in NiMnGa seven-layered martensitic phase, Appl. Phys. Lett. 80 (2002), https://doi.org/10.1063/1.1458075.
[73] C. Jiang, Y. Muhammad, L. Deng, W. Wu, H. Xu, Composition dependence on the martensitic structures of the Mn-rich NiMnGa alloys, Acta Mater 52 (2004) 2779–2785, https://doi.org/10.1016/j.actamat.2004.02.024.
[74] M. Richard, J. Feuchtwanger, D. Schlagel, T. Lograsso, S.M. Allen, R.C. O'Handley, Crystal structure and transformation behavior of Ni–Mn–Ga martensites, Scr. Mater 54 (2006) 1797–1801, https://doi.org/10.1016/j.scriptamat.2006.01.033.
[75] K. Vallal Peruman, M. Mahendran, S. Seenithurai, Effect of Mn concentration on the phase transformation in Ni-Mn-Ga single crystal, Phys. B 405 (2010) 1770–1774, https://doi.org/10.1016/j.physb.2010.01.037.
[76] C. Seguí, E. Cesari, J. Font, J. Muntasell, V.A. Chernenko, Martensite stabilization in a high temperature Ni-Mn-Ga alloy, Scr. Mater 53 (2005) 315–318, https://doi.org/10.1016/j.scriptamat.2005.04.009.
[77] S.J. Murray, M. Farinelli, C. Kantner, J.K. Huang, S.M. Allen, R.C. O'Handley, Field-induced strain under load in Ni–Mn–Ga magnetic shape memory materials, J. Appl. Phys. 83 (1998) 7297–7299, https://doi.org/10.1063/1.367758.
[78] X. Jin, M. Marioni, D. Bono, S.M. Allen, R.C. O'Handley, T.Y. Hsu, Empirical mapping of Ni-Mn-Ga properties with composition and valence electron concentration, J. Appl. Phys. 91 (2002) 8222–8224, https://doi.org/10.1063/1.1453943.
[79] O. Heczko, N. Lanska, O. Soderberg, K. Ullakko, Temperature variation of structure and magnetic properties of Ni-Mn-Ga magnetic shape memory alloys, J. Magn. Magn. Mater. (2002) 1446–1449, https://doi.org/10.1016/S0304-8853(01)01087-3, 242–245.